

Supporting information for:

**Bilayer thickness mismatch controls domain size in model membranes**

*Frederick A. Heberle, Robin S. Petruzielo, Jianjun Pan, Paul Drazba, Norbert Kučerka, Robert F. Standaert, Gerald W. Feigenson, and John Katsaras*

The supporting information consists of three stand-alone tables, and four sections containing four figures and ten equations.

**Table S1. Sample compositions, Ld mole fractions and volume fractions, and scattering length densities [ $\text{fm}/\text{\AA}^3$ ]**

Sample	$\chi_{\text{DSPC}}^{\text{a}}$	$\chi_{\text{DOPC}}$	$\chi_{\text{POPC}}$	$\chi_{\text{Chol}}$	$\rho^{\text{b}}$	$\chi_{\text{Ld}}^{\text{c}}$	$v_{\text{f,Ld}}^{\text{d}}$	$a_{\text{f,Ld}}^{\text{e}}$	SLD60 <sup>f</sup>	SLD20 <sup>g</sup>
D1	0.39	0	0.39	0.22	0	0.24	0.25	0.29	0.181	0.191
D2	0.39	0.02	0.37	0.22	5	0.27	0.28	0.32	0.181	0.191
D3	0.39	0.04	0.35	0.22	10	0.29	0.30	0.34	0.181	0.191
D4	0.39	0.06	0.33	0.22	17	0.31	0.32	0.37	0.181	0.191
D5	0.39	0.08	0.31	0.22	20	0.32	0.33	0.38	0.181	0.191
D6	0.39	0.14	0.25	0.22	35	0.35	0.36	0.43	0.181	0.190
D7	0.39	0.39	0	0.22	100	0.41	0.43	0.52	0.180	0.190
S1	0.325	0	0.325	0.35	0	N/A	N/A	N/A	0.182	0.190
S2	0	0	0.65	0.35	0	N/A	N/A	N/A	0.025	0.026

<sup>a</sup>The DSPCd<sub>70</sub>/DSPC ratio is fixed at 2:1 for all trajectory and control samples

<sup>b</sup> $\rho \equiv \chi_{\text{DOPC}} / (\chi_{\text{DOPC}} + \chi_{\text{POPC}})$  [%]

<sup>c</sup>mole fraction of Ld phase at 20 °C calculated from the phase diagram (Fig. 1)

<sup>d</sup>volume fraction of Ld phase at 20 °C calculated as a mole fraction-weighted sum of individual lipid volumes<sup>1-4</sup>

<sup>e</sup>area fraction of Ld phase at 20 °C calculated as:  $a_{\text{f,Ld}} = v_{\text{f,Ld}} / [t_{\text{ac,Ld}} / t_{\text{ac,Lo}} (1 - v_{\text{f,Ld}}) + v_{\text{f,Ld}}]$ , where  $t_{\text{ac}}$  is the acyl chain thickness of the Ld (Lo) phase

<sup>f</sup>average bilayer SLD at 60 °C (SLD of 34.6% D<sub>2</sub>O at 60 °C is 0.181)

<sup>g</sup>average bilayer SLD at 20 °C (SLD of 34.6% D<sub>2</sub>O at 20 °C is 0.184)

**Table S2. Neutron scattering lengths, molecular volumes at 60 °C, and corresponding scattering length densities of species relevant to this study**

<b>Molecule</b>	<b>Chem. Formula</b>	<b><i>b</i> [fm]</b>	<b><i>V</i> [Å<sup>3</sup>]</b>	<b>SLD [fm/Å<sup>3</sup>]</b>
PC headgroup	C <sub>10</sub> H <sub>18</sub> NO <sub>8</sub> P	60.1	331 <sup>a</sup>	0.181
DSPC chains	C <sub>34</sub> H <sub>70</sub>	-35.8	1017 <sup>b</sup>	-0.035
DSPCd <sub>70</sub> chains	C <sub>34</sub> D <sub>70</sub>	692.9	1017 <sup>b</sup>	0.681
DOPC chains	C <sub>34</sub> H <sub>66</sub>	-20.8	1003 <sup>c</sup>	-0.021
POPC chains	C <sub>32</sub> H <sub>64</sub>	-26.6	953 <sup>b</sup>	-0.028
cholesterol	C <sub>27</sub> H <sub>46</sub> O	13.3	630 <sup>d</sup>	0.021
water	H <sub>2</sub> O	-1.68	30.4	-0.055
heavy water	D <sub>2</sub> O	19.15	30.5	0.628
34.6% heavy water	H <sub>1.31</sub> D <sub>0.69</sub> O	5.53	30.4	0.181
11.7% heavy water	H <sub>1.77</sub> D <sub>0.23</sub> O	0.761	30.4	0.025

<sup>a</sup>data found in 1

<sup>b</sup>data found in 2

<sup>c</sup>data found in 3

<sup>d</sup>data found in 4

**Table S3. Tieline endpoint compositions (mole fraction), scattering length density ( $\text{fm}/\text{\AA}^3$ ), and spontaneous curvature ( $10^{-2} \text{ nm}^{-1}$ ) at 20 °C**

Sample	$\chi_{\text{DSPC}}$	$\chi_{\text{DSPCd70}}$	$\chi_{\text{DOPC}}$	$\chi_{\text{POPC}}$	$\chi_{\text{Chol}}$	SLD20	$J^a$
D1 <sub>Ld</sub>	0.03	0.06	0	0.79	0.12	0.026	-6.8
D1 <sub>Lo</sub>	0.17	0.32	0	0.26	0.25	0.251	-9.5
D2 <sub>Ld</sub>	0.03	0.06	0.04	0.75	0.12	0.026	-6.8
D2 <sub>Lo</sub>	0.17	0.33	0.01	0.24	0.25	0.258	-9.5
D3 <sub>Ld</sub>	0.03	0.06	0.08	0.71	0.12	0.026	-6.9
D3 <sub>Lo</sub>	0.18	0.33	0.02	0.21	0.26	0.265	-9.6
D4 <sub>Ld</sub>	0.03	0.06	0.13	0.66	0.12	0.026	-7.0
D4 <sub>Lo</sub>	0.18	0.34	0.04	0.18	0.26	0.273	-9.7
D5 <sub>Ld</sub>	0.03	0.06	0.16	0.63	0.12	0.026	-7.0
D5 <sub>Lo</sub>	0.18	0.35	0.04	0.17	0.26	0.276	-9.7
D6 <sub>Ld</sub>	0.03	0.06	0.28	0.51	0.12	0.027	-7.2
D6 <sub>Lo</sub>	0.19	0.36	0.06	0.12	0.27	0.289	-9.9
D7 <sub>Ld</sub>	0.03	0.06	0.79	0	0.12	0.030	-8.1
D7 <sub>Lo</sub>	0.21	0.39	0.11	0	0.29	0.319	-10.6

<sup>a</sup>calculated as a mole fraction-weighted sum of individual lipid spontaneous curvatures ( $10^{-2} \text{ nm}^{-1}$ ):  $J_{\text{DSPC}}=0$ ,  $J_{\text{DOPC}}=-5$ ,  $J_{\text{POPC}}=-3.33$ ,  $J_{\text{Chol}}=-34$  <sup>5,6</sup>

## S1. Non-domain contributions to total scattering intensity

As mentioned in the main text, the total integrated scattered intensity ( $Q = \int I(q)q^2 dq$ ) can be expressed as the sum of three components, which are related to the square of the mean SLD contrast (*i.e.*, the difference between the SLDs of bilayer and water), the mean square radial SLD fluctuations, and the mean square lateral SLD fluctuations.<sup>7</sup> Comparing the single-phase samples S1 and S2 to phase-separated trajectory samples D1–D7, it is evident that lateral contrast, and not mean or radial contrast (which to first order affect the samples equally), is the dominant source of scattering in this experiment. Nevertheless, it is instructive to estimate the relative contributions of the mean and lateral scattering components.

Over the 40 °C temperature range employed in this study, small changes in mean bilayer contrast are expected due to temperature-dependent changes in lipid volume, which are on the order of 0.1% per °C for glycerophospholipids.<sup>2</sup> We calculate that the mean bilayer contrast ( $|\text{SLD}_{\text{medium}} - \text{SLD}_{\text{bilayer}}|$ ) of both trajectory and control samples increases from  $\sim 0 \text{ fm}/\text{\AA}^3$  at 60 °C, to  $\sim 0.007 \text{ fm}/\text{\AA}^3$  at 20 °C (Table S1); for the purposes of this calculation, we will use a conservative upper-bound estimate of  $0.01 \text{ fm}/\text{\AA}^3$ . Based on tieline compositions at 20 °C, the calculated lateral contrast between  $L_0$  and  $L_d$  phase domains increases from  $0.23 \text{ fm}/\text{\AA}^3$  at composition D1 to  $0.29 \text{ fm}/\text{\AA}^3$  at composition D7 (Table S3). The lateral component is independent of domain size, but scales with the product of the domain and surround area fractions [*i.e.*,  $\alpha \times (\alpha - 1)$ , where  $\alpha$  is the domain area fraction].<sup>7</sup> A conservative estimate (25% domain surface coverage) of the relative contributions of lateral and mean components to the total scattering is therefore  $I_{\text{lat}}/I_{\text{mean}} \sim 0.25 \times 0.75 \times (0.2/0.01)^2 = 75$  (*i.e.*, 75 to 1) at 20 °C. This calculation suggests that the observed scattering is due almost entirely to the lateral component. At 20 °C, the  $\sim 4$ -fold increase in total intensity as  $\rho$  increases from 0 to 100% (Figure 4) suggests that both lateral contrast and domain area fraction increase with increasing fraction of DOPC, an observation consistent with the phase diagram of Figure 1.

## S2. Monte Carlo modeling of SANS data

### S.2.1. Methodology

SANS profiles were modeled with a modified coarse-graining method.<sup>8</sup> For the experimental conditions used in this study (*i.e.*, contrast matching of the solvent, lipid headgroups, and acyl chains), the vesicle scattering volume was approximated by a spherical shell of radius  $R$  and thickness  $t$  corresponding to the hydrophobic portion of the bilayer. For phosphocholine bilayers, the difference between the steric bilayer thickness and the hydrophobic thickness is  $\sim 10 \text{ \AA}$ ,<sup>2</sup> and the hydrophobic thicknesses of each phase were therefore estimated by subtracting  $10 \text{ \AA}$  from the measured bilayer thicknesses (Table 1). The shell volume was further divided into one or more randomly placed, non-overlapping caps (domains), each subtending an angle  $2\alpha$ . For  $N$  domains of thickness  $t_d$  comprising a combined volume fraction  $v_d$ , the domain half-angle  $\alpha$  and radius  $R_d$  are:

$$\alpha = \cos^{-1} \left( 1 - \frac{2t_s v_d}{N[t_d(1 - v_d) + t_s v_d]} \right) \quad (S1)$$

$$R_d = \alpha R \quad (S2)$$

where  $t_s$  is the thickness of the continuous bilayer surrounding the domains. Based on the sample compositions and published phase diagrams for the three-component systems, the minor phase at all trajectory compositions is the Ld phase (Table S1), and therefore the circular domains were considered to be Ld phase dispersed in a continuous Lo phase. The mole fraction of each lipid component in each phase was calculated from the ternary phase diagrams and the assumption of linear variation of tieline endpoints in the four-component space (Figure 1). The volume fraction of domain phase  $v_d$  was then calculated from the mole fractions and published lipid volumes (Table S1), and the scattering length densities (SLDs) of each phase were calculated (Table S3).

Having specified the coordinates of the domain centers and their half-angle, random coordinates were generated within the shell volume in proportion to the SLD contrasts of the phases (*i.e.*, the difference between the SLD of the phase and of the aqueous solvent). Random coordinates were chosen with a rejection algorithm, whereby coordinates were uniformly generated within the shell and tested for inclusion in a domain until both the domain and surrounding volumes accumulated the desired number of points. Figure S1 shows an example vesicle object with randomly generated coordinates. The SLD contrast-weighted pair distance distribution  $P(r)$  for the vesicle was then calculated from the set of random coordinates following Henderson.<sup>9</sup>

The average vesicle radius  $R_{av}$  and polydispersity  $\sigma$  were incorporated into the simulation as a Schulz distribution:

$$G(R) = \left(\frac{z+1}{R_{av}}\right) \frac{R^z}{\Gamma(z+1)} \exp\left[\frac{-R(z+1)}{R_{av}}\right] \quad (S3)$$

where the relative polydispersity ( $\sigma/R_{av}$ ) is  $[1/(z+1)]^{1/2}$ .  $P(r)$  were calculated as described above for a large number of vesicles ( $10^5$ ) whose individual radii  $R$  were drawn from  $G(R)$ , and the individual  $P(r)$  were summed to obtain the complete  $P(r)$  function for the polydisperse system. The scattered intensity is the Fourier transform of  $P(r)$ :

$$I(q) = \frac{1}{4\pi} \int P(r) \frac{\sin(qr)}{qr} dr \quad (S4)$$

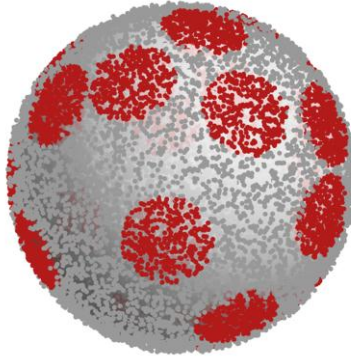


**Figure S1** Example of a Monte Carlo vesicle for calculation of the pair-distance distribution function  $P(r)$ . Random coordinates were generated within the domain (red) and surround (gray) phases in proportion to their respective SLD contrasts. Pair-distance distributions for  $10^5$  randomly generated vesicles like this one were combined to obtain an ensemble-averaged  $P(r)$ , which was then used to calculate the scattering curve *via* Equation S4.

### S.2.2. Error estimates

Uncertainty in domain size was estimated using a Monte Carlo propagation of errors that accounts for both experimental noise and uncertainty in the fixed model parameters.<sup>10</sup> A random data set with the same noise characteristics as the experimental scattering data was generated by drawing random  $I(q)$  values from normal distributions with mean intensity given by the best-fit  $I(q)$  curve, and standard deviation obtained from counting statistics (as provided by the data reduction software). This data was then fit using a similarly generated random set of fixed model parameters, to obtain a best-fit domain size value. The procedure was repeated 50 times to obtain a distribution of domain sizes, the standard deviation ( $\sigma$ ) of which is taken to be the uncertainty in domain size. The  $\pm 2\sigma$  error bars shown in Figure 7 correspond to a 95% confidence interval for the measurement.

### S.2.3. Composition D7

Unlike compositions D1–D6, composition D7 ( $\rho = 100\%$ ) was not adequately fit by a single scattering curve calculated for a fixed number of domains. The lack of an observable scattering peak (Figure 3) suggests a large domain size, but the simulated  $N = 1$  curve predicts a sharp decrease in intensity in the range  $0.005 < q < 0.012 \text{ \AA}^{-1}$ . Instead, a more gradual decrease is observed in the experimental data, shown in Figure S2:

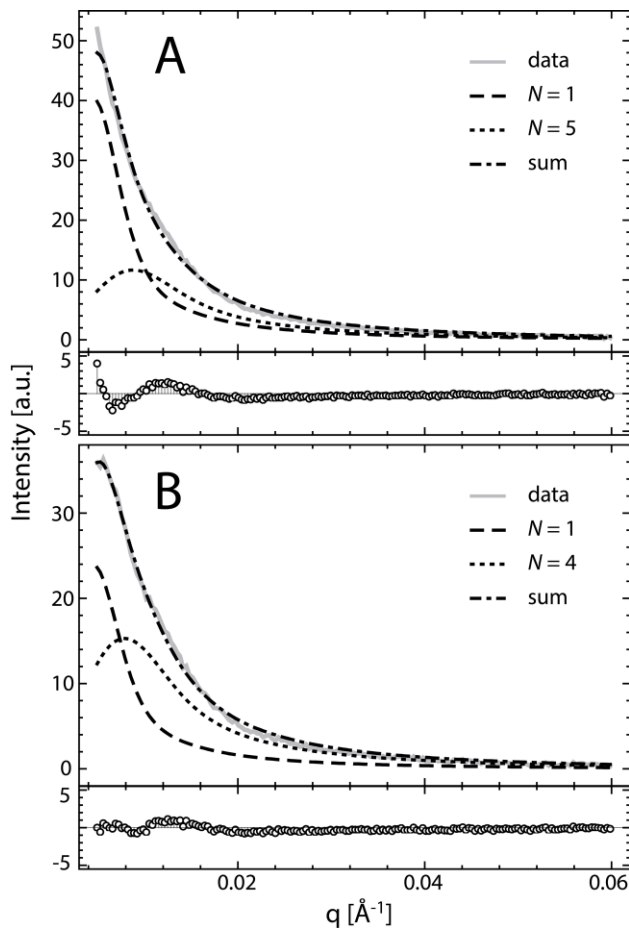


**Figure S2** Composition D7 is fit by a linear combination of Monte Carlo SANS curves. *A*, a weighted sum of curves corresponding to 1 and 5 domains provides a reasonable fit to the experimental data at 20 °C, though the residual plot reveals a poor fit at low  $q$ . *B*, after subtracting a residual scattering contribution (taken to be the 50 °C scattering curve), a better fit is achieved at low  $q$ , using a weighted sum of curves corresponding to 1 and 4 domains per vesicle.

We were able to account for the enhanced shoulder in the experimental data by fitting to a linear combination of  $N = 1$  and  $N = 5$  curves using weighting factors 0.43 and 0.57, respectively (Figure S2,A). We found that while the  $N = 1$  curve is strictly required (for any combinations excluding  $N = 1$ , a distinct peak is predicted at low  $q$  that is not seen in the data), fits of similar quality are obtained by substituting  $N = 4$  or  $N = 6$  as the second curve. In all cases, oscillations in the residual plots indicate a poor fit at low  $q$ , due to the anticipation in the  $N = 1$  curve of a scattering peak at  $q \sim 0.0045 \text{ \AA}^{-1}$ , just below the experimental  $q$  window. A better fit is achieved at low  $q$  by first subtracting the 50 °C scattering curve (where the bilayer is expected to be well mixed) from the 20 °C data to generate a SANS curve that is corrected for non-domain scattering contributions, as shown in Figure S2,B. Interestingly, a leveling-off of the corrected curve is observed at low  $q$ , consistent with the predicted curve for a single domain. A linear combination of  $N = 1$  and  $N = 4$  curves provides the best fit to the corrected data, using weighting factors 0.29 and 0.71, respectively. Though this approach provides a better fit at low  $q$ , the result is both qualitatively and quantitatively similar to the uncorrected data. Our interpretation is that vesicles at composition D7 likely contain a few (1–4) large domains, consistent with observations in GUV. The source of the residual scattering in the 50 °C data is unclear and has been previously observed in raft mixtures composed of DPPC/DOPC/Chol.<sup>8,11</sup> One potential explanation is the presence of daughter vesicles that budded from MLVs during freeze/thaw cycles.<sup>12</sup> In the case of macroscopically phase-separated bilayers, such budding would result in a small population of vesicles with single-phase Ld and Lo compositions, which cannot be contrast matched to the solvent at any temperature.

### S3. Calculations of composition-dependent line tension from theory

We applied the theory of Kuzmin et al.,<sup>13</sup> which relates domain/surround thickness mismatch, elastic moduli, and spontaneous curvature to bilayer line tension  $\gamma$ :

$$\gamma = \frac{2\sqrt{B_s K_s B_d K_d}}{\sqrt{B_d K_d} + \sqrt{B_s K_s}} \frac{\delta^2}{h_0^2} - \frac{(B_s J_s - B_d J_d)^2}{(\sqrt{B_d K_d} + \sqrt{B_s K_s})} \quad (S5)$$

where the subscripts  $s$  and  $d$  refer to surround and domain, respectively,  $\delta$  is the monolayer thickness mismatch,  $h_0$  is the average monolayer thickness of the Ld and Lo phases, and  $B$ ,  $K$ , and  $J$  are the phase-specific bending modulus, tilt modulus, and spontaneous curvature, with units of energy, energy/area, and length<sup>-1</sup>, respectively. Considering only elastic contributions to  $\gamma$  (*i.e.*,  $J_s = J_d = 0$ ) and using typical values of elastic moduli ( $B = 50 kT$ ,<sup>14</sup>  $K = 10 kT^{13}$ ), we calculate line tensions of  $\sim 2$ – $6$  pN as  $\rho$  varies from 0 to 100%. These  $\gamma$  are similar to (or larger than) experimental values of 0.5–3.5 pN obtained with micropipette aspiration experiments where macroscopic domains are observed on giant vesicles.<sup>15</sup> This suggests that elastic considerations alone predict line tensions too large to explain the experimental observation in giant vesicles of a nanoscopic phase regime for DSPC/DOPC/POPC/Chol.

To obtain a smaller line tension  $\gamma$  that might correspond to nanoscopic domains, we must take curvature into account. This is done by calculating the spontaneous curvature  $J$  for the Ld and Lo phases, as a mole-fraction weighted sum of lipid spontaneous curvatures found in the literature (Table S3). Figure S3 shows a contour plot of  $\gamma$  versus  $\rho$  (which includes the composition-dependent variation in  $\delta$  and  $J$ ) and Lo bending modulus  $B_{Lo}$ :

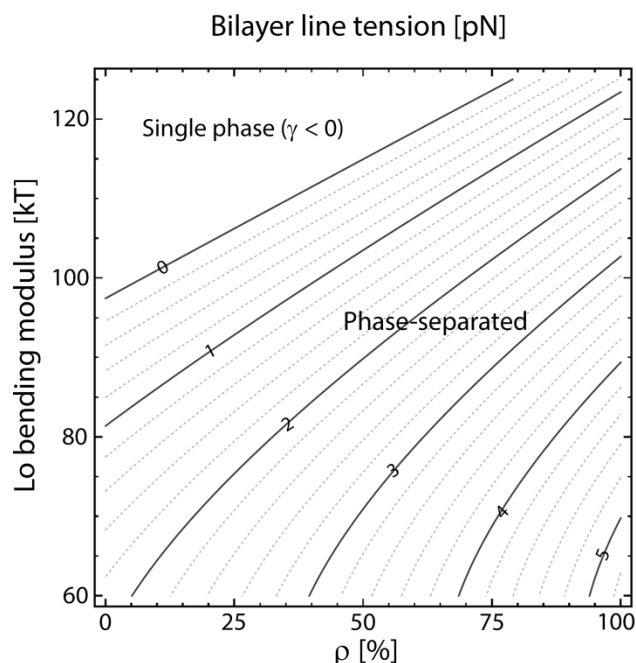


**Figure S3** Line tension calculations for DSPC/DOPC/POPC/Chol. Increasing  $\rho$  (horizontal movement on the contour plot) increases the thickness mismatch of coexisting Ld and Lo phases, resulting in a  $\sim$  quadratic increase in line tension ( $\gamma$ ) according to Equation S5. With Ld bending modulus fixed at  $50 kT$ , increasing the Lo bending modulus (vertical movement) results in an overall decrease in  $\gamma$  at fixed  $\rho$ .

If Lo and Ld are comparably flexible (lower portion of Figure S3), Equation S5 again predicts line tension values  $> 1$  pN for  $0 < \rho < 100\%$ . As  $B_{Lo}$  increases,  $\gamma$  decreases at all  $\rho$ , due to coupling between bending rigidity and spontaneous curvature (the second term in Equation S5). For large enough values of  $B_{Lo}$ ,  $\gamma$  assumes negative values (“single phase” region in Figure S3), conditions which do not favor domain formation. At intermediate values of  $B_{Lo}$ ,  $\gamma$  values near 0 are predicted at low  $\rho$ , conditions which should favor nanodomain formation.

#### S4. Asymmetric bilayer form factor

To determine bilayer thickness, we modeled the real-space scattering length density (SLD) profile of the bilayer (*i.e.*, the variation in SLD in the direction normal to the plane of the membrane).<sup>16</sup> The bilayer's SLD profile is related to the observed SANS intensity  $I(q)$  by a Fourier transform.<sup>17</sup> Flat bilayers with identical compositions on the inner and outer leaflet are centrosymmetric structures, and are consequently described by SLD profiles that are symmetric about the bilayer midplane. For centrosymmetric bilayers, SANS curves exhibit characteristic zero-intensity minima. In contrast, scattering from highly curved vesicles often show non-zero minima ("liftoff"), which is a direct consequence of asymmetry in the bilayer form factor.<sup>18</sup> For the 60 nm vesicles used in this study, a distinct liftoff is apparent in samples prepared for bilayer thickness measurements (Figure 7), indicative of some degree of structural and/or compositional asymmetry between the inner and outer leaflets. Such asymmetry is frequently observed in ULV with radii  $< 100$  nm.<sup>18-21</sup>

We modeled the bilayer structure as follows. Because the resolution of SANS data is limited, we considered only simple models of a few parameters that capture the broad features of an asymmetric SLD profile. A simple asymmetric model for protiated ULV in 100% D<sub>2</sub>O is shown schematically in Figure S4:

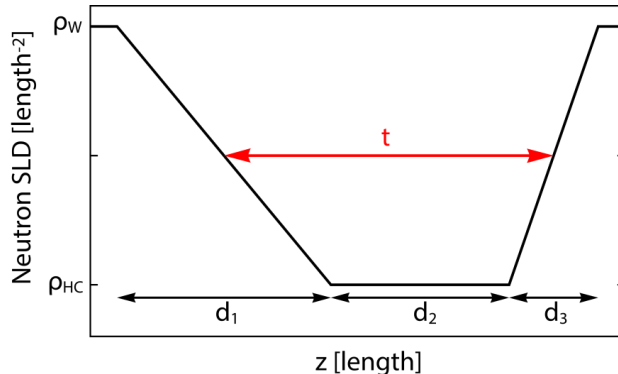


**Figure S4** A model neutron scattering length density profile for an asymmetric bilayer. Asymmetry of the inner and outer leaflets is accounted for by the independent thicknesses  $d_1$  and  $d_3$  (which cannot be unambiguously assigned to either leaflet). The total bilayer thickness  $t$  is taken to be the distance between the midpoints of the interfacial regions.

In this model, the interfacial regions  $d_1$  and  $d_3$  of the bilayer are represented by a linearly varying profile connecting the SLD of the aqueous medium ( $\rho_w$ ) to the SLD of the hydrocarbon core ( $\rho_{HC}$ ) with thickness  $d_2$ . Asymmetry is accounted for by allowing the lengths  $d_1$  and  $d_3$  to vary independently of each other. It must be emphasized that these thicknesses cannot be

unambiguously assigned to the inner or outer leaflet, and do not map in a straightforward way to structural components of the lipid. Rather, they account for radial variations in SLD that reflect both asymmetric lipid packing *and* an asymmetric radial water distribution. The mathematical model corresponding to Figure S4 is:

$$\rho(z) = \begin{cases} \frac{(\rho_{HC} - \rho_W)}{d_1} z + \rho_W & 0 < z \leq d_1 \\ \rho_{HC} & d_1 < z \leq d_1 + d_2 \\ \frac{(\rho_W - \rho_{HC})}{d_3} (z - d_1 - d_2 - d_3) + \rho_W & d_1 + d_2 < z \leq d_1 + d_2 + d_3 \\ \rho_W & z > d_1 + d_2 + d_3 \end{cases} \quad (S6)$$

The asymmetric bilayer form factor  $F(q)$  is the complete Fourier transform (with complex exponential) of the SLD profile:<sup>17</sup>

$$|F(q)| = \left( \left[ \int_0^{d_3} \Delta\rho(z) \cos(qz) dz \right]^2 + \left[ \int_0^{d_3} \Delta\rho(z) \sin(qz) dz \right]^2 \right)^{1/2} \quad (S7)$$

where  $\Delta\rho(z) = \rho(z) - \rho_w$  is the SLD contrast between the bilayer and aqueous medium. Combining Equations S6 and S7 yields an analytical expression for the form factor:

$$|F(q)| = \frac{|\rho_{HC} - \rho_W|}{d_1 d_3 q^2} \{ [d_3(1 - \cos[d_1 q]) + d_1(\cos[(d_1 + d_2 + d_3)q] - \cos[(d_1 + d_2)q])]^2 + [d_3 \sin[d_1 q] + d_1(\sin[(d_1 + d_2)q] - \sin[(d_1 + d_2 + d_3)q])]^2 \}^{1/2} \quad (S8)$$

For  $q > \sim 0.03 \text{ \AA}^{-1}$  (the range of our experimental data), the effects of vesicle size and polydispersity are negligible. In this  $q$  regime, the bilayer form factor dominates the SANS intensity, such that  $I(q) \propto |F(q)|^2$ . Accounting for a constant incoherent background  $I_{inc}$ , the final expression for SANS intensity is:

$$I(q) = A(|F(q)|^2 + I_{inc}) \quad (S9)$$

where  $A$  is a scaling factor that incorporates the bilayer SLD contrast in Equation S8, in addition to sample-to-sample concentration differences. Equation S9 has five adjustable parameters:  $A, I_{inc}, d_1, d_2$  and  $d_3$ .

We varied  $A, I_{inc}, d_1, d_2$  and  $d_3$  in a nonlinear least-squares routine, to achieve a best fit to the experimental  $I(q)$ . Best-fit curves are shown along with the experimental data in Figure 7. We define the total bilayer thickness  $t$  (red arrow in Figure S4) as the distance between the midpoints of the inner and outer interfaces:

$$t = d_2 + \frac{d_1 + d_3}{2} \quad (S10)$$

The best-fit thicknesses for Ld and Lo compositions are shown in Table 1 of the main text.

## References

- (1) Tristram-Nagle, S.; Liu, Y.; Legleiter, J.; Nagle, J. F. *Biophys. J.* **2002**, *83*, 3324.
- (2) Kučerka, N.; Nieh, M. P.; Katsaras, J. *Biochim. Biophys. Acta* **2011**, *1808*, 2761.
- (3) Tristram-Nagle, S.; Petrache, H. I.; Nagle, J. F. *Biophys. J.* **1998**, *75*, 917.
- (4) Greenwood, A. I.; Tristram-Nagle, S.; Nagle, J. F. *Chem. Phys. Lipids* **2006**, *143*, 1.
- (5) Boulgaropoulos, B.; Rappolt, M.; Sartori, B.; Amenitsch, H.; Pabst, G. *Biophys. J.* **2012**, *102*, 2031.
- (6) Szule, J. A.; Fuller, N. L.; Rand, R. P. *Biophys. J.* **2002**, *83*, 977.
- (7) Anghel, V. N. P.; Kučerka, N.; Pencer, J.; Katsaras, J. *J. Appl. Crystallogr.* **2007**, *40*, 513.
- (8) Pencer, J.; Mills, T.; Anghel, V.; Krueger, S.; Epan, R. M.; Katsaras, J. *Eur. Phys. J. E* **2005**, *18*, 447.
- (9) Henderson, S. J. *Biophys. J.* **1996**, *70*, 1618.
- (10) Press, W. H.; Teukolsky, S. A.; Vetterling, W. T.; Flannery, B. P. *Numerical Recipes in C: The Art of Scientific Computing*; 2nd ed.; Cambridge University Press: New York, 1988.
- (11) Vogtt, K.; Jeworrek, C.; Garamus, V. M.; Winter, R. J. *Phys. Chem. B* **2010**, *114*, 5643.
- (12) Nezil, F. A.; Bayerl, S.; Bloom, M. *Biophys. J* **1992**, *61*, 1413.
- (13) Kuzmin, P. I.; Akimov, S. A.; Chizmadzhev, Y. A.; Zimmerberg, J.; Cohen, F. S. *Biophys. J.* **2005**, *88*, 1120.
- (14) Semrau, S.; Idema, T.; Holtzer, L.; Schmidt, T.; Storm, C. *Phys. Rev. Lett.* **2008**, *100*, 088101.
- (15) Tian, A. W.; Johnson, C.; Wang, W.; Baumgart, T. *Phys. Rev. Lett.* **2007**, *98*, 208102.
- (16) Heberle, F. A.; Pan, J.; Standaert, R. F.; Drazba, P.; Kučerka, N.; Katsaras, J. *Eur. Biophys. J.* **2012**, *41*, 875.
- (17) Pencer, J.; Krueger, S.; Adams, C. P.; Katsaras, J. *J. Appl. Crystallogr.* **2006**, *39*, 293.

- (18) Kučerka, N.; Pencer, J.; Sachs, J. N.; Nagle, J. F.; Katsaras, J. *Langmuir* **2007**, *23*, 1292.
- (19) Kučerka, N.; Nieh, M. P.; Katsaras, J. *Langmuir* **2009**, *25*, 13522.
- (20) Brzustowicz, M. R.; Brunger, A. T. *J. Appl. Crystallogr.* **2005**, *38*, 126.
- (21) Chiantia, S.; Klymchenko, A. S.; London, E. *Biochim. Biophys. Acta* **2012**, *1818*, 1284.